Aerodynamic Optimization of Airfoil Shape for Subsonic, Transonic, Supersonic and Hypersonic Speeds

Bernardo Cardoso Leite
bernardo.leite@tecnico.ulisboa.pt

Instituto Superior Técnico, Universidade de Lisboa, Portugal

July 2022

Abstract

Hypersonic flight has been the subject of numerous research programs throughout the last eight decades. This work aims to study and optimize the aerodynamic performance of a two-dimensional baseline airfoil (NACA0012) at distinct speeds within the framework of a hypersonic transport aircraft. Hence, a mission profile has been defined, from which four points representing the subsonic, transonic, supersonic, and hypersonic flow conditions have been selected. To carry out the flow study and optimization procedures, a methodology has been implemented based on CFD simulations performed on the high-fidelity solver SU2, where RANS have been chosen as governing equations and SA as turbulence model. The computational mesh has been generated via Gmsh, followed by a Grid Convergence Study, which has ensured spatial convergence and grid-independent numerical results for each of the speed regimes. Gradient-based optimizations have been conducted using drag as the objective function to be minimized, as well as the Free-Form Deformation technique as the parameterization method. Moreover, an additional optimization for the hypersonic case has been carried out using a Genetic Algorithm approach and Local Piston Theory. The optimization results show an overall improvement in aerodynamic performance, including decreases in the drag coefficient up to 79.2%. In the end, a morphing strategy has been laid out based on the optimal shapes produced by optimizations.

Keywords: Aerodynamic Shape Optimization, Computational Fluid Dynamics, Hypersonic, SU2

1. Introduction

Air travel has become a common mode of transportation, essential to connect cities and people, as well as to develop and reinforce economic ties. According to the International Civil Aviation Organization (ICAO) [1], in 2019, the number of passengers carried in scheduled services reached the record value of approximately 4.5 billion people. Hence, the demand for new and faster technologies has translated into an increasing attention given towards hypersonic transportation, specially over the past two decades. [2]

The study of hypersonic transport aircraft is motivated by the potential to fly further and faster, thus reducing travel times and pollutant emissions. Traveling from Brussels to Sydney in about three hours [3] or crossing the pacific ocean in less than two hours [4] are two major possibilities enabled by hypersonic transportation. The growing interest in space-related industries, such as space tourism or space exploration, also contribute to the development and empowerment of hypersonic solutions.

To attain hypersonic flight conditions, an aircraft must first undergo subsonic, transonic and super-sonic speeds. Over such a wide speed range, the nature of the flow will greatly change. Consequently, the aircraft's aerodynamic responses will also vary substantially. For that reason, the design of a hypersonic vehicle must take into account the balance of aerodynamic performances over its vast flight envelope.

Taking a step further, it is desirable to optimize the aerodynamic performance of a vehicle - or two-dimensional airfoil in the case of this work -, in accordance to a set of flight conditions. Since the flight envelope is so vast, the significant variations in flow and aerodynamic performance will inevitable lead to conflicting shape design requirements. Hence, an Aerodynamic Shape Optimization (ASO) procedure is commonly carried out in the aerospace field, enabling the improvement of a body's aerodynamic performance by means of modifying its shape. [5] This procedure implies the use of parameterization techniques, which are responsible for accurately describing the body's geometry.

Finally, upon having the optimal design solutions for each flight condition, a morphing strategy can be studied and implemented, thus satisfying the

1

multi-design and conflicting requirements. Morphing mechanisms are common in nowadays aviation, e.g. flaps and slats, improving the aerodynamic performance of aircraft at distinct flight segments. [6]

The theoretical and mathematical background is presented in Section 2, followed by the methodology in Section 3, which describes the steps and procedures. In Section 4, the case study is formulated, and the results are presented in Section 5. Finally, conclusions are drawn in Section 6.

2. Background

To study the aerodynamic performance of a body, it is first necessary to properly describe the behaviour of the flow around it. By accurately modeling the behaviour of the flow, it is then possible to compute the relevant aerodynamic parameters, namely the lift and drag coefficients, C_l and C_d, respectively, as well as the lift-to-drag ratio (L/D).

2.1. Governing equations of Fluid Dynamics

The fluid is described by a set of equations, which are derived from applying the principle of conservation laws to quantities such as the momentum, energy or density. These equations are called the governing equations of fluid dynamics or, more commonly, Navier-Stokes (NS) equations. [7] Since NS are conservation equations, they hold similar structure and can be represented in differential conservative form as follows in equation (1),

$$\frac{\partial \mathbf{V}}{\partial t} + \nabla \cdot \mathbf{F}^c - \nabla \cdot \mathbf{F}^v = 0 \qquad (1)$$

where $\mathbf{V}$ represents the state variables vector, $\mathbf{F}^c$ refers to the convective fluxes, and $\mathbf{F}^v$ the viscous fluxes. Source terms have not been required. The state variables vector is presented below in (2),

$$\mathbf{V} = (\rho, \rho\mathbf{u}, \rho E)^T \qquad (2)$$

where ρ, $\mathbf{u}$ and E refer to the density, velocity vector and total energy, respectively. The convective fluxes, $\mathbf{F}^c$, are given in equation (3).

$$\mathbf{F}^c = \begin{pmatrix} \rho\mathbf{u} \\ \rho\mathbf{u}\mathbf{u} + p\mathbf{I} \\ \rho H \end{pmatrix} \qquad (3)$$

In equation (3), p and H represent the pressure and total enthalpy, respectively. $\mathbf{I}$ denotes the identity matrix. The viscous fluxes, $\mathbf{F}^v$, are presented in equation (4),

$$\mathbf{F}^v = \begin{pmatrix} \emptyset \\ \tau \\ \tau + k\nabla T \end{pmatrix} \qquad (4)$$

where k and T refer to the thermal conductivity and temperature, respectively. The sheer stress tensor is given by τ and it is presented in equation (5).

$$\tau = \mu[\nabla\mathbf{u} + (\nabla\mathbf{u})^T] - \frac{2}{3}\mu(\nabla \cdot \mathbf{u})\mathbf{I} \qquad (5)$$

In equation (5), the dynamic viscosity is represented by letter μ and computed via Sutherland's law. Overall, the set of governing equations presented in equation (1) is highly non-linear and can only be solved by computational means. In the present work, SU2 [8] is the selected high-fidelity flow solver in charge of carrying out the numerical simulations of the flow field enfolding the airfoil geometry.

2.2. Turbulence and Turbulence Model

Depending on its nature, the fluid can either be laminar or turbulent. Whereas laminar flow is characterized by a smooth and layered behaviour, turbulent flow is highly chaotic and irregular. Turbulence is a direct consequence of instabilities that arouse from laminar flows, effect of perturbations which are amplified due to the highly non-linear inertial terms. [9, 10]

The computational cost of simulating and solving the entire length of turbulence scales via direct numerical solution (DNS) would be unattainable. Hence, to overcome the issue posed by turbulent flows and their unsteadiness, a time-average procedure is carried out on NS equations. This decomposition of time-dependent variables into mean and fluctuating terms, leads to the derivation of the Reynolds-Averaged Navier-Stokes (RANS) equations. However, RANS equations introduce new unknowns, via the stress tensor τ, causing a closure problem. This closure problem is overcomed by the introduction of a turbulence model. [7]

A turbulence model predicts the evolution of turbulence, being capable of modeling the turbulent scales and structures. In the present work, the Spalart-Allmaras (SA) [11] one-equation turbulence model is selected to compute the the turbulent viscosity parameter. Therefore, the SU2 [8] solver employs the RANS equations closed by the SA turbulence model to describe the behaviour of the flow around the airfoil geometry for the distinct flight conditions.

2.3. Finite Volume Method

The Finite Volume Method (FVM) consists of subdividing the numerical domain into a finite and discrete number of control volumes (CV), over which the the governing equations are integrated, yielding the discretized equations at the CVs' nodal points. [12]

SU2 [8] uses the vertex-centered approach for variable arrangements, where the grid points are used as nodal points for the construction of the CV. Moreover, SU2 uses a median-dual technique, where

the CV are built around grid points by connecting the cells' face-midpoints to the cell's centroids. Consequently, a dual grid is generated. Figure 1 illustrates, in a simplified fashion, a primal grid designed by the user, and then a dual grid composed by all the CVs and automatically generated by SU2.
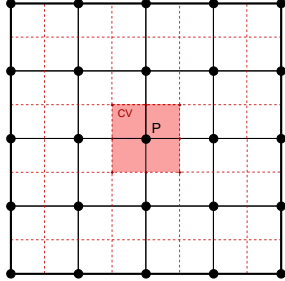

Figure 1: Illustration of both the primal grid (black continuous line) and dual grid (red dashed line).

The governing equations are integrated over the dual grid, where the Gauss Theorem is applied to the volume integrals associated with the convective and diffusive terms, converting them into surface integrals. These surface integrals can be rewritten in the form of sums. Using the notation presented in [8], the semi-discretized typical partial differential equation (PDE) is presented as follows:

$$\int_{\Omega_i} \frac{\partial \mathbf{V}}{\partial t} d\Omega + \sum_{j \in \mathcal{N}(i)} (\tilde{F}^c_{ij} + \tilde{F}^v_{ij}) \Delta S_{ij} = \int_{\Omega_i} \frac{\partial \mathbf{V}}{\partial t} d\Omega + \mathcal{R}_i(V) = 0 \tag{6}$$

where Ω represents the numerical domain, $\mathcal{N}(i)$ is the set of neighboring grid points to grid point i, $\tilde{F}^c_{ij}$ and $\tilde{F}^d_{ij}$ are the numerical approximations of the convective and viscous fluxes, respectively. ΔS_{ij} defines the area of the face associated with the edge ij and $\mathcal{R}_i(V)$ represents the numerical residuals representing the integration of all spatial terms at grid point i.

2.4. Local Piston Theory

Piston Theory is a technique used to compute the pressure around thin and slender bodies, e.g. airfoils, under hypersonic flow conditions. This theory provides good results with respect to the pressure distribution. Hence, by applying its linearized form to a local flow field, it is possible to derive the Local Piston Theory (LPT) [13], presented below in equations (7).

$$\begin{cases} p = p_l + \rho_l a_l W_l \\ W_l = \mathbf{u}_l \cdot \delta\mathbf{n} + \mathbf{u}_b \cdot \mathbf{n} \\ \delta\mathbf{n} = \mathbf{n}_0 - \mathbf{n} \end{cases} \tag{7}$$

The variables p_l, ρ_l, a_l, and u_l represent the local pressure, density, speed of sound, and flow velocity, respectively. W denotes the local downwash speed, which is given by the sum of both the geometrical deformation ($\mathbf{u}_l \cdot \delta\mathbf{n}$) and vibration ($\mathbf{u}_b \cdot \mathbf{n}$). Lastly, $\mathbf{n}$ refers to the outward normal unit vector after deformation and $\mathbf{n}_0$ the outward unit vector before deformation.

3. Methodology

Methodology comprises the strategies and steps undertaken throughout the present work in order to produce a feasible and accurate framework for both the baseline and optimization simulations.

3.1. Airfoil Geometry & Mesh Design

The first step addresses the geometrical framework, that is, the set-up of the computational domain, which includes airfoil geometry and domain's boundaries, followed by the mesh design and generation.

NACA0012, presented in Figure 2, is selected as the baseline geometry, given the great amount of experimental and numerical data available, as well as its worldwide use in validation and optimization problems. NACA0012 is a symmetrical airfoil, therefore has no camber, and produces null lift at zero angle of attack (AoA). Its maximum thickness of 12% is located at 30% of the chord. In the present work, the airfoil coordinates are computed and then written in Gmsh [14] format using MATLAB.
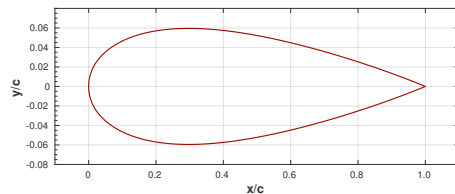

Figure 2: NACA 0012 airfoil geometry.

The design of the mesh is performed in Gmsh [14], an open-source software with CAD-built capabilities. The meshing process takes into account several factors, including: the airfoil geometry, the important physical phenomena that needs to be properly captured, the boundary conditions, and, finally, the computational cost. Moreover, mesh quality is guaranteed by ensuring smoothness, alignment, and low values of skewness throughout the mesh.
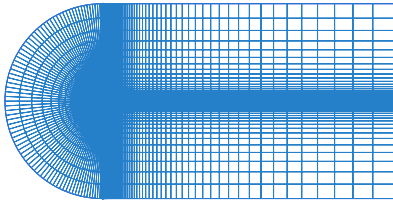
The overall structure of this work's primal grid is displayed in Figure 3(a), containing information regarding the grid dimensions and growth factors. The mesh itself is presented in Figure 3(b).

3.2. Grid Convergence Study (GCS)

In order to ensure grid-independent numerical solutions and spatial convergence, a GCS is carried
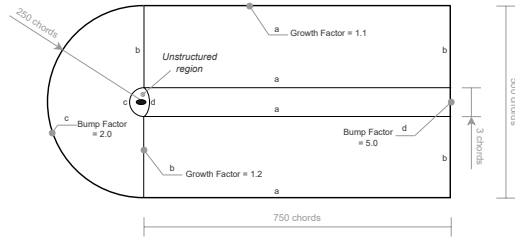
(a) Overall mesh strategy.

(b) General view of the mesh.

Figure 3: Mesh strategy and generation.

out for all speed regimes, from subsonic to hypersonic. In the present work, each study performs CFD steady-state simulations on five successively finer grids. The grid refinement ratio, r, is equal to 2, and spatial convergence has been proved for all cases, as presented in Figure 4.
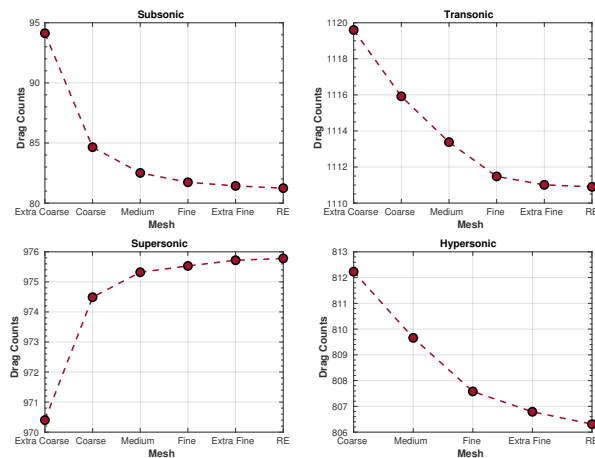

Figure 4: GCS for the four speed regimes.

Furthermore, the Richardson Extrapolation (RE) [15] method has been employed to obtain a higher-order estimate of the solution value when the grid spacing is equal to zero. This value is also presented in Figure 4, and the relative error between the RE estimation and the value of the medium mesh is lower than 2% for all cases. Given the small relative error and lower computational cost in comparison to finer grids, the medium mesh has been selected for the baseline and optimization simulations, with exception of the hypersonic case, where the extra fine mesh is chosen due to convergence issues.

3.3. SU2 solver

SU2 is an open-source, computational analysis and design software, whose core tools are compiled C++ executables used to discretize and solve problems described by PDEs. SU2 is capable of solving complex, multi-physics and optimization problems. In addition to that, this high-fidelity solver includes geometric parameterization tools and mesh deformations techniques, essential to optimization procedures. In the present work, all baseline simulations, as well as the gradient-based optimizations are run in the high-fidelity SU2 solver.

3.4. Baseline Simulations

Baseline simulations are steady-state CFD simulations performed for each of the different flight conditions, which are presented in Section 4. Problem Formulation. These simulations hold great importance since their numerical solutions - including aerodynamic data - are used as baseline comparison with respect to the optimization results.

3.5. Optimization Simulations

One of the main objectives regarding the present work is to optimize the NACA0012 airfoil geometry, so that better aerodynamic performance may be achieved for a given flight condition. Hence, a proper optimization framework is fundamental. In the current work, two paths are chosen with respect to optimization procedures:

A Gradient-Based Method (GBM) - developed within the SU2 framework and the main choice for optimization procedure. This procedure is applied to all speed regimes, from subsonic to hypersonic.

B Genetic Algorithm (GA) - a gradient-free technique that is used together with the Local Piston Theory for optimization at the hypersonic regime.

A. Gradient-Based Optimizations

GBM are commonly employed in the design of aerospace vehicles, in which the vehicle shape - or airfoil shape in the case of the present work - is parameterized with a set of design variables. These methods compute the gradients of the objective function with respect to the design variables, thus defining better search directions, and, ultimately, reach an optimal design solution. The Discrete Adjoint Method [16] is already implemented within SU2, and selected as GBM for optimization procedure. Moreover, the Free-Form Deformation (FFD) [17] parameterization technique is employed.

The flowchart containing the detailed gradient-based optimization procedure is illustrated in Figure 5.
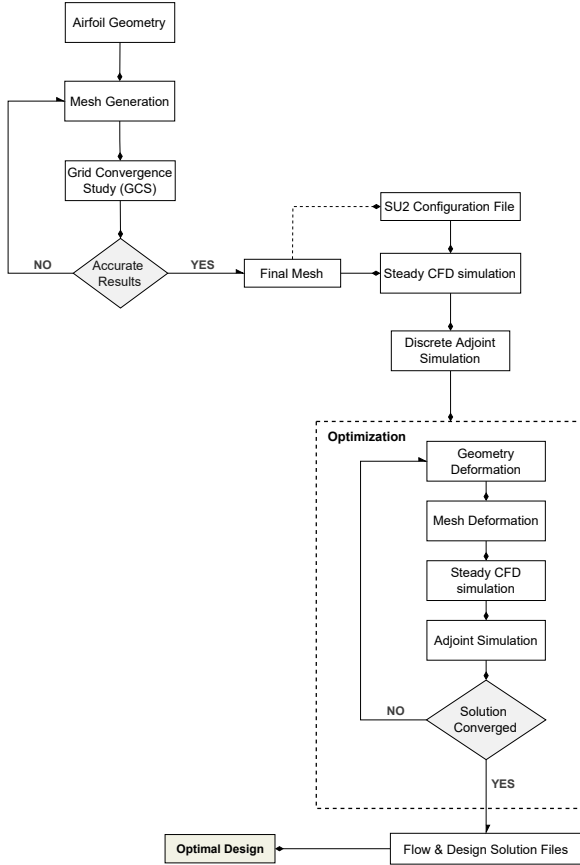
4

Figure 5: Gradient-based optimization flowchart.

B. Genetic-Algorithm Optimization

The Non-dominated Sorting Genetic Algorithm II (NSGA-II) [18], already developed and implemented in MATLAB, is subject to modification to properly include the Local Piston Theory (LPT) and the Class Shape Transformation (CST) [19] parameterization scheme. The LPT is used to determine the new values of pressure along the airfoil surface, after its deformation. Both the lift and drag coefficients are computed using this information. The CST technique describes each airfoil surface individually by means of a Bernstein polynomial of order 6. This corresponds to 7 independent design variables for each surface, 14 altogether.

Note that a GA is an evolutionary optimization technique based on some of the natural processes that take place in biological evolution. By employing tools such as selection, crossover and mutation operators, GA attempts to mimic the natural selection, thus leading the evolution of an initial population towards an optimal solution. [20]

The flowchart comprising detailed information regarding the GA-based optimization procedure is presented in Figure 6.
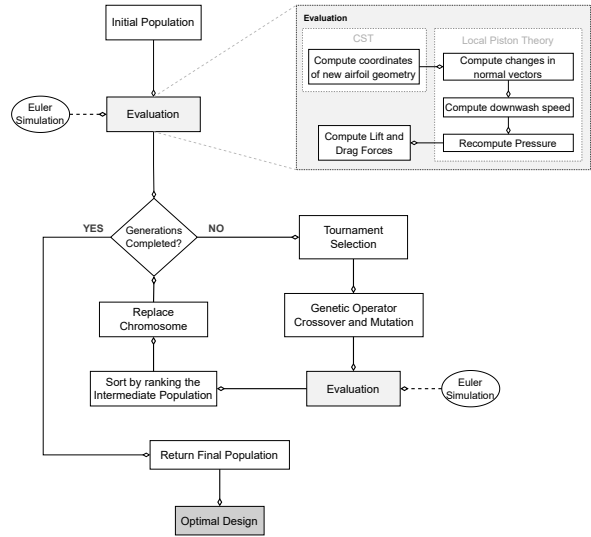

Figure 6: Gradient-based Optimization Flowchart.

4. Problem Formulation

The goal is to assess and optimize the aerodynamic performance of two-dimensional NACA0012 airfoil for different speed regimes, within the framework of a hypothetical hypersonic transport aircraft.

4.1. Mission Profile

The mission profile is presented below in Figure 7, and consists of a simplified description of the distinct flight segments, which are then associated with a given altitude and speed ranges. This mission profile has been produced in a similar fashion to the STRATOFLY [21] project's mission profile.
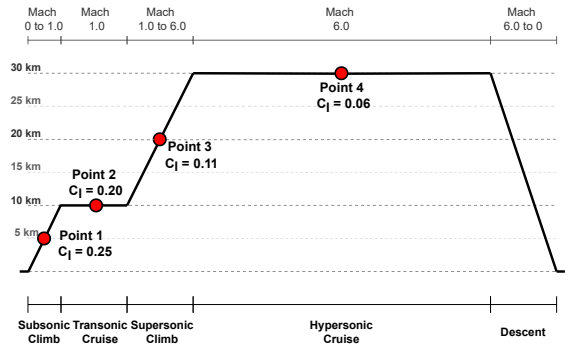

Figure 7: Mission Profile.

As shown in Figure 7, four points have been selected to proceed with analysis and optimization. The lift coefficient (C_l) values indicated on the figure are the target values for optimization.

In Table 1 is presented the main information with respect to each of these points. As one may observe, each of them represents a distinct speed regime, at different altitude and temperature. The Reynolds

Table 1: Main information regarding selected points.

Point	Speed Regime	Mach	Altitude (km)	Temperature (K)	Density (Kg/m^3)	Reynolds (Re)
1	Subsonic	0.5	5	255.65	0.7364	$7.25 \cdot 10^6$
2	Transonic	1.0	10	223.25	0.4135	$8.49 \cdot 10^6$
3	Supersonic	2.0	20	216.65	0.0889	$3.69 \cdot 10^6$
4	Hypersonic	6.0	30	226.65	0.0184	$2.26 \cdot 10^6$

number (Re) is greater than 10^6 for all cases, thus stipulating that the flow is turbulent. [7] Moreover, the type of the boundary conditions (BC) applied in this work is presented in Table 2. The values of the Farfield BC vary in accordance to the free-stream properties of each flight condition. The Heat Flux BC is equal for all cases, indicating that the airfoil surface is an adiabatic, no-slip wall.

Table 2: Boundary Conditions.

Boundary Condition	Application
Farfield	Domain's Boundary
Heat Flux	Airfoil

The convergence criteria for all the CFD simulations run in SU2 is the root mean square of the density residual. The threshold of convergence varies for each simulation case, depending on its speed regime, since convergence more difficult to reach as the flow speed increases. [9] That said, the density residual must be lower than 10^{-11}, 10^{-11}, 10^{-9} and 10^{-5} for the subsonic, transonic, supersonic, and hypersonic cases, respectively. Moreover, the other residuals must also be inferior to 10^{-4}.

4.2. Baseline Simulations

In this work, five baseline simulations have been run in SU2 to assess the flow field and extract the main aerodynamic coefficients of NACA0012 airfoil at different flight conditions.

Four of these baseline simulations correspond to each of the aforementioned points, presented in Table 1. Their results are then compared to the gradient-based optimization results.

The fifth baseline simulation has been run for the hypersonic case, yet using Euler instead of RANS as governing equations. Euler equations are a simplification of the NS equations, where the flow is considered both inviscid and adiabatic. This fifth simulation is essential for the GA-based optimization procedure, since it provides the local values for the LPT.

4.3. Optimization Simulations

A. Gradient-Based Optimizations

Four optimization simulations have been carried

out in SU2 using the discrete adjoint method. Each of these optimizations correspond to one of the selected points presented in Table 1. Regarding the parameterization technique, a FFD box has been wrapped around the airfoil geometry employing a total of 24 design variables equally spaced, as presented in Figure 8.
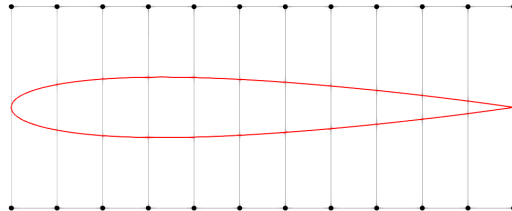

Figure 8: FFD box.

The optimization formulation is presented below,

$$
\begin{aligned}
\min \quad & C_d \\
\text{w.r.t.} \quad & \mathbf{X} = [X_1, X_2, \ldots, X_{24}] \\
\text{s.t.} \quad & C_l = C_l(\text{target}) \\
& \text{Airfoil\_thickness} \geq 0.0012 \\
& \text{Airfoil\_area} \geq 0.0545 \\
& \text{Airfoil\_LE\_radius} \leq 30000
\end{aligned} \tag{8}
$$

where the drag coefficient (C_d) is the objective function to be minimized, with respect to the 24 design variables $\mathbf{X}$, and subject to lift constraint and three airfoil geometrical constraints. Note that LE radius refers to the radius of the leading edge.

B. Genetic-Algorithm Optimization

One optimization simulation has been performed for the hypersonic case using the NSGA-II algorithm in MATLAB. The number of generations is selected as convergence criteria, being sufficiently large to ensure complete convergence towards an optimal solution. An initial population of 350 individuals has been set-up, and the optimization process has taken a total of 2000 generations.

The optimization formulation is presented below,

$$
\begin{aligned}
\min \quad & C_d \,;\, C_d/C_l \\
\text{w.r.t.} \quad & \mathbf{X} = [X_1, X_2, \ldots, X_{14}] \\
\text{s.t.} \quad & X_1 = X_8
\end{aligned} \tag{9}
$$

where two objective functions have been defined, both the drag coefficient (C_d) and the drag-to-lift ratio (C_d/C_l), with respect to the 14 design variables $\mathbf{X}$, and subject to a design constraint forcing the continuity at the leading edge region.

5. Results

The optimization results are addressed and compared to the baseline results. The optimal shapes are presented, as well as the pressure and temperature distributions along the chord. In the end, a morphing strategy is discussed.

5.1. Gradient-Based Optimizations

The results with respect to the main aerodynamic coefficients, C_l and C_d, are presented in Table 4. The first major difference is the production of lift by the optimized shapes, with the exception of the hypersonic case. The lift targets are satisfied for the subsonic, transonic and supersonic cases. Moreover, with the production of lift, the optimized shapes present non-zero lift-to-drag ratio (L/D). The L/D comparison is presented below in Table 3, where for the subsonic case there is a large increase, and then, as expected, the L/D decreases with the increase in speed.

Table 3: Lift-to-Drag ratio results.

Point	Speed Regime	Lift-to-Drag (L/D)	
		Baseline	Optimization
1	Subsonic	0.00	29.20
2	Transonic	0.00	2.97
3	Supersonic	0.00	2.69
4	Hypersonic	0.00	0.00

Regarding the drag coefficient, results show a substantial decrease of 39.5%, 46.5% and 79.2% in the transonic, supersonic and hypersonic cases, respectively. The subsonic results show a small increase of 1.81%, which can be justified by the induced drag caused by generation of lift and due to the fact that NACA0012 is already a good shape for subsonic speeds.
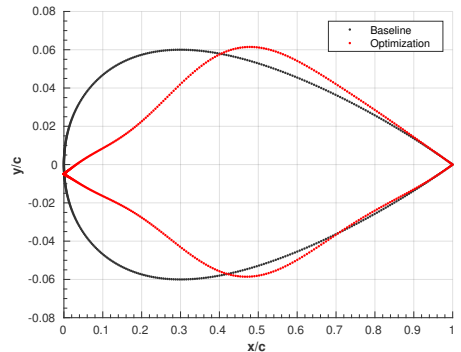
The comparison between the baseline and optimized shapes is presented in Figure 9. The subsonic results (Figure 9(a)) reinforce the statement that NACA0012 is a suitable geometry for low-speeds, since its geometrical variation is very small. However, the transonic results show great differences in shape design between the optimization and baseline geometries (Figure 9(b)). The leading edge region is stretched outwards and then, around $x = 0.2$, pushed a little inwards, resembling the shape of a whale. Furthermore, there is a displacement of maximum thickness towards the back of the airfoil.
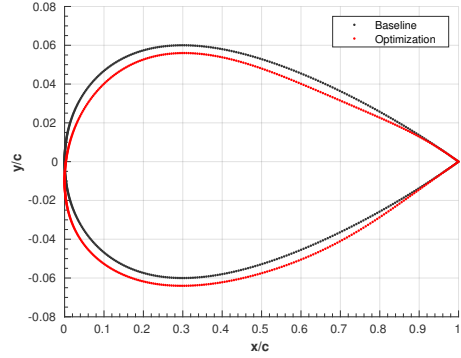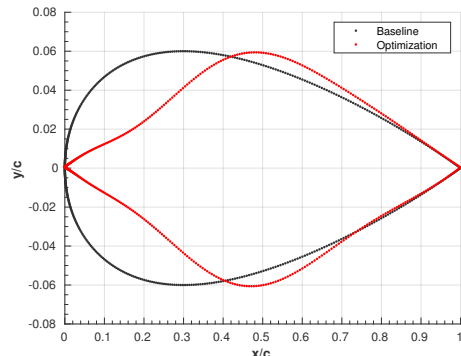

(a) Subsonic Case, Mach=0.5
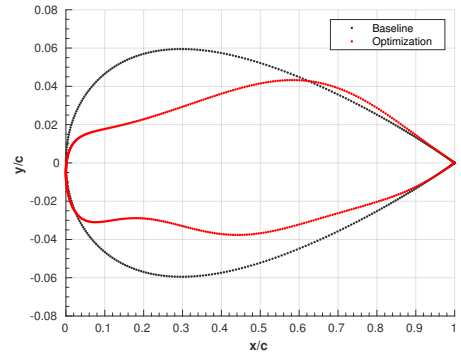
(b) Transonic Case, Mach=1.0

(c) Supersonic Case, Mach=2.0

(d) Hypersonic Case, Mach=6.0

Figure 9: Comparison between Baseline and Optimized airfoil shapes.

7

Finally, in both supersonic (Figure 9(c)) and hypersonic (Figure 9(d)) results, the optimal design greatly differs from the baseline one. The region comprising the leading edge is pulled inwards, significantly decreasing the LE radius. In addition to that, the position corresponding to the maximum thickness is moved from $x/c = 0.3$ to $x/c \approx 0.5$, in both cases. These optimal designs resemble a biconvex or double wedge airfoil, which is expected for such high speeds. [22]
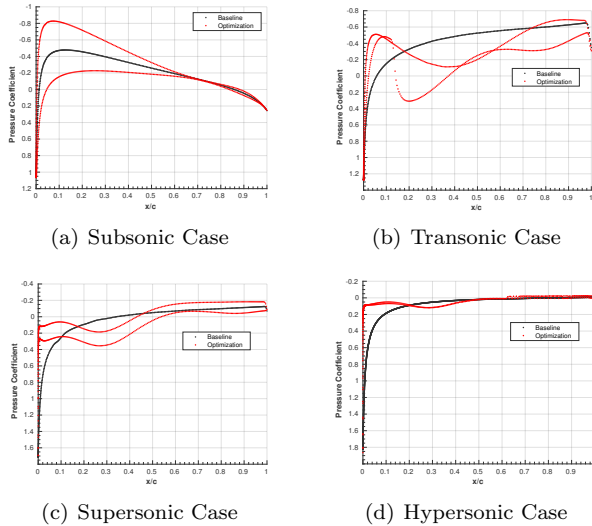

(a) Subsonic Case   (b) Transonic Case

(c) Supersonic Case   (d) Hypersonic Case

Figure 10: Comparison between Baseline and Optimized Pressure Coefficient distributions.

The distribution of the pressure coefficient, C_p, along the chord is presented in Figure 10 for all cases. The baseline distributions display a smooth behaviour, where both the upper and lower surfaces show similar values of C_p. However, as lift is generated by the optimized shapes, C_p is expected to show differences between the upper and lower surfaces. These gaps are visible in the subsonic, transonic and supersonic cases, as predicted. Moreover, it is important to point out that in both the transonic and supersonic cases, there are sudden variations of C_p, mainly in the transonic case, which translate into the presence of shock waves. Nonetheless, the overall drag coefficient is still greatly reduced, as previously mentioned.

In the hypersonic environment, temperature plays an important role. A body subject to hypersonic speeds is confronted with very high temperatures, as well as great temperature gradients. These temperatures can be prejudicial to the body's structural integrity, and enable chemical reactions in the flow around, such as dissociation and ionization. [22] The temperature comparison between the baseline and optimization results is presented in Figure 11. The subsonic (Figure 11(a)), transonic (Figure 11(b)), and supersonic (Figure 11(c)) cases,

show small temperature variations between the upper and lower surfaces, and along x/c. In addition to that, for the subsonic and transonic cases, temperatures are lower than 270 K, and for the supersonic case, lower than 400 K. However, this pattern significantly changes for the hypersonic case (Figure 11(d)), where temperatures reach a maximum of 1905.6 K at the stagnation point, and large variations - in the order of 600 K - take place along the airfoil surface. The lowest temperatures, around 1320 K, are observed at the trailing edge region.
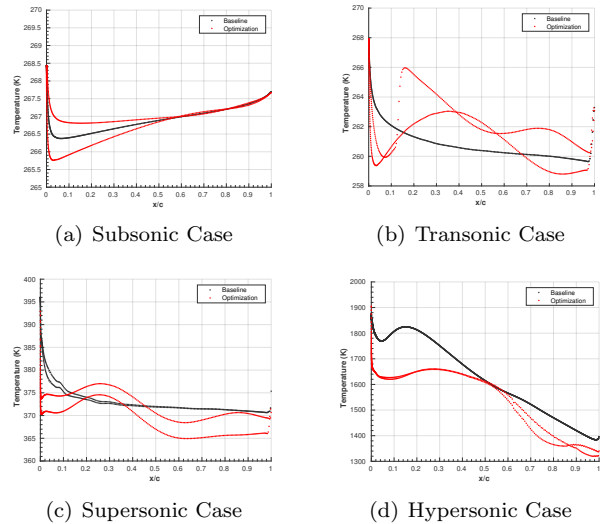

(a) Subsonic Case   (b) Transonic Case

(c) Supersonic Case   (d) Hypersonic Case

Figure 11: Comparison between Baseline and Optimized Temperature distributions.

5.2. Genetic Algorithm Optimization

The results regarding the GA-based optimization for the hypersonic case, where the hypersonic Euler simulation is taken as the baseline solution, show a decrease of 3.17% in the drag coefficient. Note that the Local Piston Theory is the biggest constrain to the optimization process, since it only allows for small geometrical variations in order to be considered valid.

Although the C_d reduction might appear small, it already starts to provide some insight into what an optimum solution should evolve to. That is, in Figure 12, a clear tendency of decrease the airfoil's thickness is observed. This tendency is both expected and desired, and further reduction is only restricted by the design variables' upper and lower bounds.

5.3. Morphing Strategy

In Figure 13, the optimal designs with respect to the four flight points analyzed are compared between each other and to the NACA0012 baseline geometry. One may easily observe that the airfoil shape significantly changes as the speed regime

8

Table 4: Comparison between baseline and gradient-based optimization aerodynamic coefficients.

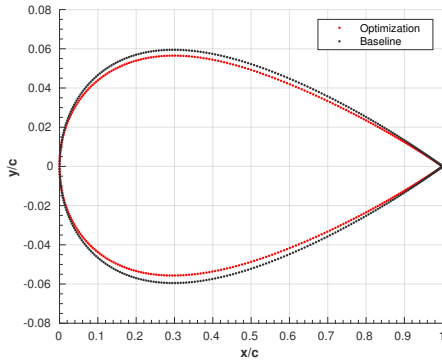| Point	Speed Regime	Lift Coefficient (C_l)			Drag Coefficient (C_d)		
		Baseline	Optimization	ΔC_l	Baseline	Optimization	$\Delta C_d (\%)$
1	Subsonic	0.00	0.25	**+0.25**	0.008407	0.008559	**+1.81%**
2	Transonic	0.00	0.20	**+0.20**	0.111338	0.067349	**-39.5%**
3	Supersonic	0.00	0.11	**+0.11**	0.097532	0.052138	**-46.5%**
4	Hypersonic	0.00	0.00	**0**	0.080679	0.016742	**-79.2%**

Figure 12: Comparison between baseline and optimization airfoil geometry.

increases, and distances itself from the subsonic speeds. Therefore, in order to perform sufficiently well, or even excel, throughout the flight envelope, the airfoil shape must adapt.
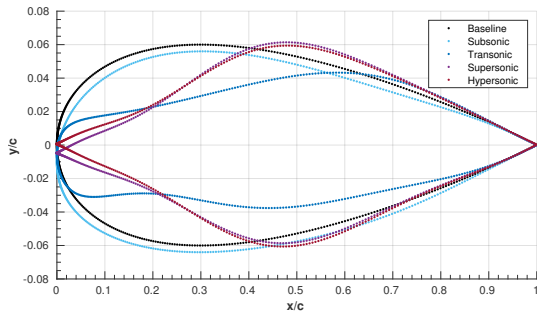

Figure 13: Baseline and optimized airfoil design geometries: overlap and comparison.

By carefully observing Figure 13, it is possible to deduce two major tendencies, or patterns, essential to lay out a first morphing strategy. The first tendency observed refers to the airfoil thickness in the first third of the chord, $x/c \leq \frac{1}{3}$. In this region, thickness is decreased as the speed increases from subsonic to hypersonic. Consequently, the maximum thickness is displaced to the right, near $x/c \approx 0.5$. In addition to that, the leading edge radius also gets increasingly smaller as the speed increases, moving towards a biconvex-like shape. Therefore, a mechanism capable of push-

ing and pulling the surface within a certain degree would carry on the required changes. The second pattern concerns the trailing edge region, which exhibits almost no change throughout the optimizations for the distinct flight conditions. Therefore, it is possible, and even advantageous structure-wise, to fix part of the airfoil geometry.
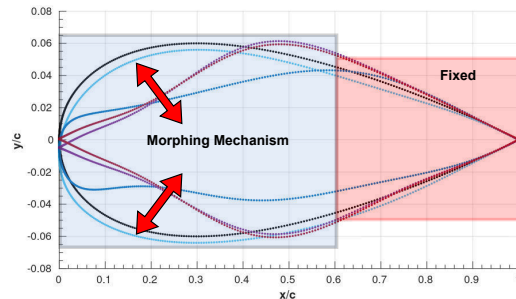

Figure 14: Final morphing strategy.

The final morphing strategy presented in Figure 14 establishes two regions. One fixed sector starting from $x/c = 0.6$ associated with the airfoil's aft region including the trailing edge. And one movable region, where an eventual elastic skin of the airfoil may be pushed both in- and outwards to satisfy the design requirement of a given flight point.

6. Conclusions

The present work led to the development of a suitable methodology that aggregates hypersonic flight and aerodynamic shape optimization. This framework translated into the performance of high-accuracy CFD flow analysis on an airfoil for distinct flight points associated with different speed regimes, including hypersonic. These flow analysis were taken one step further by means of implementing an optimization framework, capable of reshaping the airfoil geometry to improve its aerodynamic parameters and produce an optimal design under the specific flight conditions and restrictions. Results have shown great promises in regards of drag reduction, up to 79.2%. Lift requirements have also been satisfied for all flight points, except for the hypersonic case, which should be further investigated.

References

[1] ICAO. Annual Report. `https://www.icao.int/annual-report-2019/Documents/ARC_2019_Air%20Transport%20Statistics.pdf`, 2019. [Online, accessed 24-04-2021].

[2] F. Liu, Z. Han, Y. Zhang, K. Song, W. Song, F. Gui, and J. Tang. Surrogate-based aerodynamic shape optimization of hypersonic flows considering transonic performance. *Aerospace Science and Technology*, 93, 2019.

[3] Periodic Reporting for Period 1 - STRATOFLY. `https://cordis.europa.eu/project/id/769246/reporting/it`. [Online, accessed 18-06-2021].

[4] H. Taguchi, H. Kobayashi, T. Kojima, A. Ueno, S. Imamura, M. Hongoh, and K. Harada. Research on hypersonic aircraft using pre-cooled turbojet engines. *Acta Astronautica*, 73:164–172, 2012.

[5] S.N. Skinner and H. Zare-Behtash. State-of-the-art in aerodynamic shape optimisation methods. *Applied Soft Computing*, 62:933–962, 2018.

[6] T. A. Weisshaar. Morphing Aircraft Systems: Historical Perspectives and Future Challenges. *Journal of Aircraft*, 50(2):337–353, 2013.

[7] J. D. Anderson. *Fundamentals of Aerodynamics*. McGraw-Hill, 5th edition, 2011.

[8] F. Palacios and et al. Stanford University Unstructured: An open-source integrated computational environment for multi-physics simulation and design. In *51st AIAA Aerospace Sciences Meeting including the New Horizons Forum and Aerospace Exposition*, 2013.

[9] F. Moukalled, L. Mangani, and M. Darwish. *The Finite Volume Method in Computational Fluid Dynamics*. Fluid Mechanics and Its Applications. Springer, Cham, 2016.

[10] A.N. Kolmogorov. The Local Structure of Turbulence in incompressible viscous fluids at very large Reynolds numbers. *Doklady Akademiia Nauk SSSR*, 30:301–305, 1941.

[11] P. Spalart and S. Allmaras. A One-Equation Turbulence Model for Aerodynamic Flows. *AIAA*, 439, January 1992.

[12] H.K. Versteeg and W. Malalasekera. *An Introduction to Computational Fluid Dynamics: The Finite Volume Method*. Pearson Education Limited, 2nd edition, 2007.

[13] W. Zhang, Z. Ye, C. Zhang, and F. Liu. Supersonic flutter analysis based on a local piston theory. *AIAA Journal*, 47(10):2321–2328, 2009.

[14] C. Geuzaine and J. Remacle. Gmsh: a three-dimensional finite element mesh generator with built-in pre- and post-processing facilities. *International Journal for Numerical Methods in Engineering*, 79:1309–1331, September 2009.

[15] L. Richardson and R. Glazebrook. IX. The approximate arithmetical solution by finite differences of physical problems involving differential equations, with an application to the stresses in a masonry dam. *Philosophical Transactions of the Royal Society of London. Series A, Containing Papers of a Mathematical or Physical Character*, 210(459-470):307–357, 1911.

[16] S. Nadarajah and A. Jameson. A Comparison of the Continuous and Discrete Adjoint Approach to Automatic Aerodynamic Optimization. *AIAA journal*, November 2014.

[17] T. Sederberg and S. Parry. Free-form deformation of solid geometric models. volume 20, pages 151–160, August 1986.

[18] A. Seshadri. NSGA - II: A multi-objective optimization algorithm, 2022. [Online, retrieved 14-03-2022].

[19] B. Kulfan and J. Bussoletti. "Fundamental" Parametric Geometry Representations for Aircraft Component Shapes. In *11th AIAA/ISSMO Multidisciplinary Analysis and Optimization Conference: The Modeling and Simulation Frontier for Multidisciplinary Design Optimization*, Portsmouth, Virginia, USA, September 2006.

[20] D. Goldberg. *Genetic Algorithms in Search, Optimization and Machine Learning*. Addison-Wesley Longman Publishing Co., Inc., USA, 1st edition, 1989. ISBN: 978-0-201-15767-5.

[21] M. Marini and P. Roncioni. Aerodynamic and aerothermodynamic challenges for the design of a hypersonic civil transport. von Karman Institute for Fluid Dynamics - Lecture Series, 2021. May 25, 2021.

[22] J.D. Anderson. *Hypersonic and High Temperature Gas Dynamics*. AIAA education series. American Institute of Aeronautics and Astronautics, 2nd edition, 2006.